Photogrammetry Applied to Wind Tunnel Testing

AIAA Journal, Vol. 38, No. 6, June 2000, pp. 964-971

Tianshu Liu[‡], L. N. Cattafesta III, and R. H. Radeztsky

High Technology Corporation, Hampton, VA 23666

A. W. Burner

NASA Langley Research Center, MS 236, Hampton, VA 23681-0001

[‡] Currently, NASA Langley Research Center, MS 238, Hampton, VA 23681-2199
Phone: (757) 864-4639, Fax: (757) 864-4799
e-mail: t.liu@larc.nasa.gov

Abstract

In image-based measurements, quantitative image data must be mapped to three-dimensional object space. Analytical photogrammetric methods, which may be used to accomplish this task, are discussed from the viewpoint of experimental fluid dynamicists. The Direct Linear Transformation (DLT) for camera calibration, used in pressure sensitive paint, is summarized. An optimization method for camera calibration is developed that can be used to determine the camera calibration parameters, including those describing lens distortion, from a single image. Combined with the DLT method, this method allows a rapid and comprehensive in-situ camera calibration and therefore is particularly useful for quantitative flow visualization and other measurements such as model attitude and deformation in production wind tunnels. The paper also includes a brief description of typical photogrammetric applications to temperature- and pressure-sensitive paint measurements and model deformation measurements in wind tunnels.

1. Introduction

Flow visualizations and videometric (or video photogrammetric) measurements produce data in the form of images. In general, an image is the result of a perspective projection of a three-dimensional object to two dimensions. In contrast to "qualitative" flow visualization methods, "quantitative" techniques seek to extract numerical data from images. In many instances, the precise location of a point in three-dimensional space is required, in addition to the value of some quantity at that location. When the rendered object is significantly three-dimensional, simple image processing schemes, such as polynomial warping, may not be sufficient. In general, photogrammetric methods can be used to determine the relationship between three-dimensional object coordinates and corresponding two-dimensional image coordinates [1-3]. This field was originally developed to determine topography using aerial photography with metric cameras. Due largely to the rapid development of CCD video cameras and computer, photogrammetric methods using these techniques have been applied recently to numerous non-topographic applications. However, photogrammetric techniques, while not in general widespread use in wind tunnel tests, have been used recently for luminescent paint and model deformation measurements. Donovan et al. [4], Bell and McLachlan [5], and Le Sant and Merienne [6] have described the application of these methods to luminescent paint imaging. In addition, photogrammetric measurements of model deformation in wind tunnels have been reviewed by Burner et al. [7] and Liu et al. [8]. Perhaps because of the difficulties associated with using the terminology of a different discipline, the application of non-topographic photogrammetry to quantitative flow visualization, while straightforward conceptually and quite useful, may be filled with pitfalls. In this paper, an optimization method for rapid and comprehensive camera calibration is developed that is particularly suitable to photogrammetric applications for wind tunnel testing since productivity is not negatively impacted. In addition, results of applying photogrammetry to temperature- and pressure-sensitive paints (TSP and PSP) and model deformation measurements are presented.

2. Collinearity Equations

Image-based measurement techniques extract data from two-dimensional (2D) images and map them into three-dimensional (3D) object space. Photogrammetry provides a

relationship between 3D coordinates in object space and corresponding 2D coordinates in images [1-3]. The fundamental problem is to determine object space coordinates (X,Y,Z) given the corresponding image coordinates (x,y). Figure 1 illustrates the camera imaging process. The lens of the camera is modeled by a single point known as the perspective center, the location of which in object space is (X_c, Y_c, Z_c). Likewise, the orientation of the camera is characterized by three Euler orientation angles. The orientation angles and location of the perspective center are referred to in photogrammetry as the exterior orientation parameters. The object point, perspective center and image point lie along a straight line for a "perfect" camera. This relationship is described by the collinearity equations, the fundamental equations of photogrammetry. On the other hand, the relationship between the perspective center and the image coordinate system is defined by the camera interior orientation parameters, namely, the camera principal distance c and the photogrammetric principal-point location (x_p, y_p). The principal distance, which equals the camera focal length for a camera focused at infinity, is the perpendicular distance from the perspective center to the image plane, whereas the photogrammetric principal-point is where a perpendicular line from the perspective center intersects the image plane. Due to lens distortion, however, perturbations to the imaging process lead to departures from collinearity that can be represented by the shifts *dx* and *dy* of the image point from its "ideal" position on the image plane. The shifts *dx* and *dy* are modeled and characterized by a number of lens distortion parameters.

In photogrammetric applications for wind tunnel testing, high contrast fiducial targets are usually placed on a model surface to determine the relationship between image and object space coordinates. The image and object space coordinates of the targets are related by the collinearity condition in which the image vector is aligned with the vector from the perspective center to the object point

$$\begin{pmatrix} x_n - x_p + dx \\ y_n - y_p + dy \\ -c \end{pmatrix} = \ddot{e}\, \boldsymbol{M} \begin{pmatrix} X_n - X_c \\ Y_n - Y_c \\ Z_n - Z_c \end{pmatrix}, \qquad (1)$$

where $\boldsymbol{M}$ is the rotation matrix, l is a scale factor, and $\boldsymbol{p}_n = (x_n, y_n)^T$ and $\boldsymbol{P}_n = (X_n, Y_n, Z_n)^T$ are the image and object space coordinates of the *nth* target, respectively. Algebraic manipulation of (1) yields the well-known collinearity equations (with the distortion terms *dx* and *dy*) relating the *nth* target location in object space to the corresponding point on image plane,

$$x_n - x_p + dx = -c\frac{m_{11}(X_n - X_c) + m_{12}(Y_n - Y_c) + m_{13}(Z_n - Z_c)}{m_{31}(X_n - X_c) + m_{32}(Y_n - Y_c) + m_{33}(Z_n - Z_c)} = -c\frac{U}{W},$$

$$, \qquad (2)$$

$$y_n - y_p + dy = -c\frac{m_{21}(X_n - X_c) + m_{22}(Y_n - Y_c) + m_{23}(Z_n - Z_c)}{m_{31}(X_n - X_c) + m_{32}(Y_n - Y_c) + m_{33}(Z_n - Z_c)} = -c\frac{V}{W}$$

where m_{ij} $(i, j = 1, 2, 3)$ are the elements of the rotation matrix $\boldsymbol{M}$ that are functions of the Euler orientation angles (w, f, k),

$$
\begin{aligned}
m_{11} &= \cos f \cos k \\
m_{12} &= \sin w \sin f \cos k + \cos w \sin k \\
m_{13} &= -\cos w \sin f \cos k + \sin w \sin k \\
m_{21} &= -\cos f \sin k \\
m_{22} &= -\sin w \sin f \sin k + \cos w \cos k \\
m_{23} &= \cos w \sin f \sin k + \sin w \cos k \\
m_{31} &= \sin f \\
m_{32} &= -\sin w \cos f \\
m_{33} &= \cos w \cos f .
\end{aligned} \tag{3}
$$

The orientation angles (w, f, k) are essentially the pitch, yaw, and roll angles of the camera in the established coordinate system. The terms *dx* and *dy* are the image coordinate shifts induced by lens distortion. The lens distortion terms can be modeled by the sum of the radial distortion and decentering distortion [9, 10]

$$
d x = d x_r + d x_d \text{ and } d y = d y_r + d y_d , \tag{4}
$$

where, assuming the optical axis of the lens is perpendicular to the image plane

$$
\begin{aligned}
d x_r &= K_1 (x_n' - x_p) r^2 + K_2 (x_n' - x_p) r^4 , \\
d y_r &= K_1 (y_n' - y_p) r^2 + K_2 (y_n' - y_p) r^4 , \\
d x_d &= P_1 [r^2 + 2(x_n' - x_p)^2] + 2P_2 (x_n' - x_p)(y_n' - y_p) , \\
d y_d &= P_2 [r^2 + 2(y_n' - y_p)^2] + 2P_1 (x_n' - x_p)(y_n' - y_p) , \\
r^2 &= (x_n' - x_p)^2 + (y_n' - y_p)^2 .
\end{aligned} \tag{5}
$$

Here, K_1 and K_2 are the radial distortion parameters, P_1 and P_2 are the decentering distortion parameters, and *x'* and *y'* are the undistorted coordinates in image. When the lens distortion is small, the unknown undistorted coordinates can be approximated by the known distorted coordinates, i.e., $x_n' \approx x_n$ and $y_n' \approx y_n$. For large distortion, iterative procedures can be employed to determine the appropriate undistorted coordinates to improve the accuracy of the estimate. The following iterative relations are used: $(x_n')^0 = x_n$ and $(y_n')^0 = y_n$, $(x_n')^{k+1} = x_n + d x[(x_n')^k, (y_n')^k]$ and $(y_n')^{k+1} = y_n + d y[(x_n')^k, (y_n')^k]$, where the superscripted iteration index is $k = 0, 1, 2 \cdots$.

The collinearity equations (2) contain the camera parameters to be determined by calibration. The parameter sets (w, f, k, X_c, Y_c, Z_c), (c, x_p, y_p), and (K_1, K_2, P_1, P_2) in (2) are the exterior orientation, interior orientation, and lens distortion parameters of a camera respectively. Analytical camera calibration techniques utilize the collinearity equations and distortion terms to determine these camera parameters [11, 12]. Since Eq. (2) is non-linear, iterative methods of least squares estimation have been used as a standard technique for the solution of the collinearity equations in photogrammetry [1-3]. However, direct recovery of the

interior orientation parameters is often impeded by inversion of a nearly singular normal-equation-matrix of the least-squares problem. The singularity of the normal-equation-matrix mainly results from strong correlation between the exterior and interior orientation parameters.

In order to reduce the correlation between these parameters and enhance the determinability of (c, x_p, y_p), the use of multiple camera stations, varying image scales, different camera roll angles and a well-distributed target field in three dimensions has been suggested by Fraser [9, 13]. Nevertheless, the multiple-station, multiple-image method for camera calibration is not easy to use in wind tunnels where only a limited number of windows are available for cameras and the positions of cameras are fixed. Thus, a single-image method of on-the-job camera calibration is desirable. The optimization method described in section 4 is a single-image, automatic camera calibration method that eliminates the singularity problem.

3. Direct Linear Transformation

The Direct Linear Transformation (DLT), originally proposed by Abdel-Aziz and Karara [14], can be very useful for determining initial values of the parameters. The DLT equations can be obtained by simply rearranging and combining terms of the collinearity equations, i.e.,

$$\begin{aligned} L_1 X_n + L_2 Y_n + L_3 Z_n + L_4 - (x_n + dx)(L_9 X_n + L_{10} Y_n + L_{11} Z_n + 1) = 0 \\ L_5 X_n + L_6 Y_n + L_7 Z_n + L_8 - (y_n + dy)(L_9 X_n + L_{10} Y_n + L_{11} Z_n + 1) = 0 \end{aligned} \quad . \tag{6}$$

The DLT parameters $L_1, \cdots L_{11}$ are related to the camera exterior and interior orientation parameters (w, f, k, X_c, Y_c, Z_c) and (c, x_p, y_p) [1]. Unlike the standard collinearity equations (2), the DLT equations (6) are linear for the DLT parameters when the lens distortion terms *dx* and *dy* are neglected. The matrix form of the linear DLT equations for *M* targets is $\boldsymbol{BL} = \boldsymbol{C}$, where $\boldsymbol{L} = (L_1, \cdots L_{11})^T$, $\boldsymbol{C} = (x_1, y_1, \cdots x_M, y_M)^T$, and $\boldsymbol{B}$ is the $2M \times 11$ configuration matrix that can be directly obtained from Eq. (6) (see reference 15). A least-squares solution for $\boldsymbol{L}$ (without requiring an initial guess) is formally given by $\boldsymbol{L} = (\boldsymbol{B}^T \boldsymbol{B})^{-1} \boldsymbol{B}^T \boldsymbol{C}$.

The DLT method is widely used in both non-topographic photogrammetry and machine vision because of its simplicity. It is also used for pressure sensitive paint measurements [5]. When *dx* and *dy* cannot be ignored, however, iterative solution methods are still needed and the DLT method loses its simplicity. In general, the DLT method can be used to obtain fairly good values of the exterior orientation parameter and the principal distance, although it gives poor estimations of the principal-point location (x_p, y_p) [15]. However, the DLT method is very useful since initial approximations can be found for other methods such as the optimization method described below that can be used for a more comprehensive calibration.

4. Optimization Method

In order to develop a simple and robust method for camera calibration, the singularity problem must be dealt with when solving the collinearity equations. An optimization method is proposed based on the following insight. A strong correlation between the interior and exterior orientation parameters leads to a singularity of the normal-equation-matrix in the least-squares problem for the full set of the camera parameters. Therefore, to eliminate the singularity, the least-squares estimation is used only for the exterior orientation parameters, while the interior orientation and lens distortion parameters are calculated separately using an optimization

method. The optimization method contains two separate, but interacting procedures: resection for the exterior orientation parameters and optimization for the interior orientation and lens distortion parameters.

4.1 Resection for the exterior orientation parameters

When the image coordinates (x_n, y_n) are in pixels, the collinearity equations (2) are expressed as

$$\begin{aligned} f_1 &= S_h x_n - x_p + dx + cU/W = 0 \\ f_2 &= S_v y_n - y_p + dy + cV/W = 0 \end{aligned}, \tag{7}$$

where S_h and S_v are the horizontal and vertical pixel spacings (mm/pixel) of a CCD camera, respectively. In general, the vertical pixel spacing is fixed and known for a CCD camera, but the effective horizontal spacing may be variable depending on the frame grabber used to digitize the image. Thus, an additional parameter, the pixel-spacing-aspect-ratio S_h / S_v, is introduced. We define $\boldsymbol{\Theta}_{ex} = (\omega, \varphi, \kappa, X_c, Y_c, Z_c)^T$ for exterior orientation parameters and $\boldsymbol{\Theta}_{in} = (c, x_p, y_p, K_1, K_2, P_1, P_2, S_h / S_v)^T$ for the interior orientation and lens distortion parameters. For given values of $\boldsymbol{\Theta}_{in}$, and sets of $\boldsymbol{p}_n = (x_n, y_n)^T$ and $\boldsymbol{P}_n = (X_n, Y_n, Z_n)^T$, $\boldsymbol{\Theta}_{ex}$ in Eq. (7) can be found by an iterative least-squares solution, referred to in photogrammetry as "resection". The linearized collinearity equations for targets $(n = 1, 2, \cdots, M)$ are written as $\boldsymbol{V} = \boldsymbol{A}(\Delta\boldsymbol{\Theta}_{ex}) - \boldsymbol{l}$, where $\Delta\boldsymbol{\Theta}_{ex}$ is the correction term for the exterior orientation parameters, $\boldsymbol{V}$ is the $2M \times 1$ residual vector, $\boldsymbol{A}$ is the $2M \times 6$ configuration matrix, and $\boldsymbol{l}$ is the $2M \times 1$ observation vector. The elements of $\boldsymbol{A}$ and $\boldsymbol{l}$ are presented in the Appendix. A least-squares solution to minimize the residuals $\boldsymbol{V}$ for the correction term is $\Delta\boldsymbol{\Theta}_{ex} = (\boldsymbol{A}^T\boldsymbol{A})^{-1}\boldsymbol{A}^T\boldsymbol{l}$. In general, the 6×6 normal-equation-matrix $(\boldsymbol{A}^T\boldsymbol{A})$ can be inverted without singularity since the interior orientation and lens distortion parameters are not included in the least-squares estimation. To obtain such $\boldsymbol{\Theta}_{ex}$ that the correction term becomes zero, the Newton-Raphson iterative method is used for solving the non-linear equation $(\boldsymbol{A}^T\boldsymbol{A})^{-1}\boldsymbol{A}^T\boldsymbol{l} = \boldsymbol{0}$ for $\boldsymbol{\Theta}_{ex}$. This approach converges over considerable ranges of the initial values of $\boldsymbol{\Theta}_{ex}$.

Therefore, for a given $\boldsymbol{\Theta}_{in}$, the corresponding exterior orientation parameter $\boldsymbol{\Theta}_{ex}$ can be obtained and are symbolically expressed as

$$\boldsymbol{\Theta}_{ex} = \boldsymbol{RESECTION}(\boldsymbol{\Theta}_{in}). \tag{8}$$

At this stage, the exterior orientation parameters $\boldsymbol{\Theta}_{ex}$ obtained from (8) are not necessarily correct unless the given interior orientation and lens distortion parameters $\boldsymbol{\Theta}_{in}$ are accurate. Obviously, an extra condition is needed to obtain correct $\boldsymbol{\Theta}_{in}$ and the determination of $\boldsymbol{\Theta}_{in}$ is coupled with the resection for $\boldsymbol{\Theta}_{ex}$. The following section describes an optimization problem to obtain the correct $\boldsymbol{\Theta}_{in}$.

4.2 Optimization for the interior orientation and lens distortion parameters

In order to determine the correct values of $\boldsymbol{\Phi_{in}}$, an extra condition must be given. We note that the correct values of $\boldsymbol{\Phi_{in}}$ are intrinsic constants of a camera/lens system, and they are independent of the target locations $\boldsymbol{p}_n = (x_n, y_n)^T$ and $\boldsymbol{P}_n = (X_n, Y_n, Z_n)^T$. Mathematically, $\boldsymbol{\Phi_{in}}$ is an invariant under a transformation $(\boldsymbol{p}_n, \boldsymbol{P}_n) \mapsto (\boldsymbol{p}_m, \boldsymbol{P}_m)$ $(m \neq n)$. By rearranging the collinearity equations with distortion terms, $\boldsymbol{\Phi_{in}}$ can be expressed in the following form

$$\begin{pmatrix} c \\ x_p \\ y_p \end{pmatrix} = \begin{pmatrix} \dfrac{-W[(S_h x_n - x_p + dx) + (S_v y_n - y_p + dy)]}{U + V} \\ S_h x_n + dx + cU/W \\ S_v y_n + dy + cV/W \end{pmatrix} = \boldsymbol{G}(\boldsymbol{p}_n, \boldsymbol{P}_n, \boldsymbol{\Phi_{in}}, \boldsymbol{\Phi_{ex}}). \quad (9)$$

Therefore, for correct values of $\boldsymbol{\Phi_{in}}$, the quantity $\boldsymbol{G}(\boldsymbol{p}_n, \boldsymbol{P}_n, \boldsymbol{\Phi_{in}}, \boldsymbol{\Phi_{ex}})$ is an invariant under the transformation $(\boldsymbol{p}_n, \boldsymbol{P}_n) \mapsto (\boldsymbol{p}_m, \boldsymbol{P}_m)$ $(m \neq n)$. In other words, for correct values of $\boldsymbol{\Phi_{in}}$, the standard deviation of $\boldsymbol{G}(\boldsymbol{p}_n, \boldsymbol{P}_n, \boldsymbol{\Phi_{in}}, \boldsymbol{\Phi_{ex}})$ calculated over all targets should be zero, i.e., $\boldsymbol{std(G)} = [\sum_{n=1}^{M} (\boldsymbol{G} - <\boldsymbol{G}>)^2 / (M-1)]^{1/2} = \boldsymbol{0}$, where $\boldsymbol{std}$ denotes the standard deviation and $<\boldsymbol{G}>$ denotes the mean value. Furthermore, since $\boldsymbol{std(G)} \geq \boldsymbol{0}$ is always valid, the correct $\boldsymbol{\Phi_{in}}$ must correspond to the global minimum point of the function $\boldsymbol{std(G)}$. Hence, the determination of correct $\boldsymbol{\Phi_{in}}$ becomes an optimization problem to seek values of $\boldsymbol{\Phi_{in}}$ that minimize the objective function $\boldsymbol{std(G)}$, i.e., $\boldsymbol{std(G)} \rightarrow min$. To solve this multiple-dimensional optimization problem, the sequential golden section search technique is used because of its robustness and simplicity [16]. Since the quantity $\boldsymbol{G}(\boldsymbol{p}_n, \boldsymbol{P}_n, \boldsymbol{\Phi_{in}}, \boldsymbol{\Phi_{ex}})$ is related to $\boldsymbol{\Phi_{ex}}$, the optimization for $\boldsymbol{\Phi}_{in}$ is coupled with the resection for $\boldsymbol{\Phi_{ex}}$. Other appropriate objective functions may also be used. An obvious choice is the root-mean-square (rms) of the residuals of calculated object space coordinates of all targets. In fact, we find that the use of $std(x_p)$ or $std(y_p)$ in optimization is qualitatively equivalent to the use of the rms of the residuals.

In principle, any component of $\boldsymbol{std(G)} = [std(c), std(x_p), std(y_p)]^T$ can be used as an objective function since minimizing one of three components simultaneously leads to minimization of other components. As will be shown, $std(x_p)$ and $std(y_p)$ have a simpler topological structure near the global minimum point than $std(c)$. Hence, $std(x_p)$ and $std(y_p)$ are more appropriate objective functions for optimization. For example, consider a simulated 3D field of targets on a step configuration shown in Fig. 2. A typical topological structure of $std(x_p)$ is shown in Fig. 3 near the global minimum point $(c, x_p, y_p) = (28, 0.2, 0.08)$ mm for simulated image of the target field. Clearly, near the global minima $std(x_p) = 0$, $std(x_p)$ exhibits a single "valley" structure such that the optimization problem is well defined. The function $std(y_p)$ has a similar topological structure in the parametric space.

Generally, the topological structure of $std(x_p)$ or $std(y_p)$ depends on three-dimensionality of the target field. For the step target field, the step height H characterizes the three-dimensionality. Figure 4 shows the topological structures of $std(x_p)$ for $H = 6$ and 2 inches. Note that the two surfaces are partially in contact. Evidently, stronger three-dimensionality of the target field with a larger H produces a steeper "valley" in topology. From the standpoint of optimization, stronger three-dimensionality leads to faster convergence. Figure 5 shows typical convergence processes of the principal distance for three different step heights. Other camera parameters have similar convergence behavior. Clearly, strong three-dimensionality of the target field improves convergence rates. For a planar field of targets $(H = 0)$, the optimization method does not generally converge to the true values. Hence, the optimization method requires a 3D target field.

The topological structure of $std(x_p)$ or $std(y_p)$ can also be affected by random disturbances on the targets. To simulate this effect, the target coordinates in the image are disturbed by mathematically adding a zero-mean random disturbance with a Gaussian distribution. Figure 6 shows the topological structures of $std(x_p)$ at disturbance levels of 1 ìm and 6 ìm (these disturbance levels correspond to 0.08 and 0.46 pixels for a typical CCD video camera system). The flattening of the sharp "valley" near the minimum point implies that noise in the image leads to a slower convergence rate and produces larger errors in the optimization computations. Figure 7 shows typical errors of the interior orientation parameters (c, x_p, y_p) as functions of the disturbance level, where the correct simulated values of (c, x_p, y_p) are $(28, 0.2, 0.08)$ (mm). For a typical CCD video camera, for example, the random error in the target centroid measurement is usually less than 0.3 mm (0.023 pixels). Thus, the corresponding predicted precision error in the estimated values of (c, x_p, y_p) by the optimization method is no more than 0.02 mm.

The optimization method still requires appropriate initial values to obtain a converged solution even though its convergence ranges of the initial values are quite large. The DLT can provide initial approximate values of the exterior orientation parameters $(\grave{u}, \ddot{o}, \hat{e}, X_c, Y_c, Z_c)$ and the principal distance c, where the domain of $(\grave{u}, \ddot{o}, \hat{e})$ is defined as $-180^0 \le \omega \le 180^0$, $-90^0 \le \phi \le 90^0$ and $-180^0 \le \kappa \le 180^0$. Using the initial approximations given by the DLT, the optimization method gives more accurate estimates of the camera orientation and lens distortion parameters. The standard optimization technique such as the golden section search method can be used to minimize the objective function $std(x_p)$ in the parametric space $(c, x_p, y_p, K_1, K_2, P_1, P_2, S_h / S_v)$. Combined with the DLT, the optimization method allows a rapid and comprehensive automatic camera calibration to obtain 14 camera parameters from a single image without requiring a guess of the initial values.

4.3 Laboratory calibrations

Camera calibrations for an Hitachi CCD camera with a Sony zoom lens (12.5 to 75 mm focal length) and an 8 mm Cosmicar television lens were made in the laboratory in order to evaluate the accuracy of the optimization method. The measurement system consisted of a CCD camera, a personal computer with a Matrox Pulsar frame-grabber board, a step target

plate, and software. A novel target-tracking program developed by High Technology Corporation was used to track targets and compute target centroids [8]. The CCD array size of the Hitachi camera was 8mm by 6mm. The digitized image size was 640 by 480 pixels with vertical and horizontal pixel spacings equal to 13.0 *mm* and 12.9 *mm*, respectively. The random error in the measurement of target centroids was less than 0.3 *mm* (0.023 pixels). The 3D target field for camera calibration was provided by a three-step target plate with 54 circular retro-reflective targets of 0.5 in diameter, a 2.0 in step height H and 2.0 in spacing between neighboring targets (Figure 8). The coordinates of the targets on the plate were measured *a priori* with a three-dimensional coordinate machine with an accuracy of 0.001 inch.

For comparison, optical techniques described by Burner *et al*. [17, 18] were also used for calibration. The laser-illuminated, displaced-reticle technique was used to determine the horizontal and vertical pixel spacing. The principal-point location was found by the unexpanded, laser-illumination technique, and the lens distortion parameters were determined from images of a calibration plate suitably aligned with the camera axis. Figure 9 shows the principal distance given by the optimization method versus zoom setting for the Sony zoom lens. Figures 10 shows the principal-point location and radial distortion coefficient K_1 as a function of the principal distance for the Sony zoom lens. The error bars in the principal-point location are determined based on replication calibration data using the optimization method collected at different camera roll angles and positions over two days. The results obtained by the optimization method are in reasonable agreement with those given by Burner [18] for the same lens. The optimization method was also used to calibrate the Hitachi CCD camera with an 8 *mm* Cosmicar television lens. Table 1 lists the interior orientation and lens distortion parameters obtained by the optimization method that are consistent with those obtained by the optical techniques. The accuracy of camera calibration is usually represented by the residual of the image coordinate calculation. Typically, the optimization method has a residual of one micron or less in the image plane for an 8mm by 6mm CCD array, depending on the accuracy of the coordinates of the target plate.

5. Applications

Photogrammetry is required in image-based measurement techniques that seek to extract data from 2D images and map them to 3D object space. Some typical applications of photogrammetry to temperature- and pressure-sensitive paints and model deformation measurements are described. Photogrammetry is also useful for other global flow visualization and measurement techniques such as particle tracking velocimetry and particle image velocimetry [19, 20].

5.1 Temperature- and pressure-sensitive paints

Temperature- and pressure-sensitive paints (TSP and PSP) are global techniques for surface temperature and pressure measurements [21, 22]. Photogrammetry is an important element of the data reduction process since TSP and PSP data in images must be mapped onto a model surface in 3D object space. Donovan et al. [4], Bell and McLachlan [5], and Le Sant and Merienne [6] have described PSP mapping using photogrammetry. In applications of photogrammetry to TSP and PSP, the collinearity equations are used for mapping after the camera is calibrated. Known object space coordinates (X, Y, Z) are mapped into unknown

image coordinates (x, y), and then TSP and PSP data at the image points are associated with the corresponding points in object space. Here, a photogrammetric application to boundary layer transition detection on a three-dimensional model is presented. A TSP system has been developed for the purpose of transition detection and applied to several three-dimensional models over a wide speed range [23]. TSP detects transition by visualizing the temperature change caused by different heat transfer rates in laminar and turbulent flow regimes in a transient thermal process. A key element of the system development has been photogrammetric tools for mapping temperature to a three-dimensional grid of the model surface. Figure 11 shows a transition image of a swept-wing model in Mach 3.5 flow mapped onto the half of the model surface grid by using photogrammetry. The bright region corresponds to the turbulent boundary layer where the heat transfer rate is higher than that in the laminar boundary layer. The onset of transition is demarcated in the image as a bright parabolic band on the wing where the cross-flow instability mechanism dominates the transition process. However, no transition is observed near the centerline of the model. This is because near the symmetric plane of the model the stability is dominated by the Tollmien-Schlichting instability mechanism that is weaker than the cross-flow instability mechanism. Detailed experimental and computational studies of transition physics on the swept-wing model at Mach 3.5 are described in references 23, 24 and 25.

5.2 Model deformation measurement

Model deformation data are required to understand the aeroelastic properties of a model and correctly interpret measured aerodynamic data for a deformed model. An optical measurement technique is the videogrammetric model deformation (VMD) method. In contrast to the applications to TSP and PSP, the collinearity equations are used in a VMD system to determine spatial coordinates of targets on a model surface from target centroids in the image plane in order to compute model deformation (twist and bending) produced by aerodynamic loads. Burner et al. [7] and Liu et al. [8] have described in detail the VMD systems used in NASA facilities, including cameras, lights, targets, image acquisition, and software for data reduction. Here, an example is presented of a model deformation measurement using a single-camera VMD system for a 72in semi-span high-lift model in the NASA Ames 12-Ft pressure tunnel. Mach number ranged from 0.23 to 0.3, dynamic pressure ranged from 140 to 330 psf, Reynolds number ranged from 2.9 to 6.73 million per foot, and angle-of-attack ranged from -6 to 23 degrees. Figure 12(a) shows the wing twist as a function of the angle-of-attack (AOA) at different spanwise locations. The magnitude of twist increases with AOA until aerodynamic stall occurs roughly at an AOA of 15 degrees. Figure 12(b) shows the bending of the wing at different AOAs. Dynamic deformation measurements were also made in the laboratory on a rectangular wing with a 44 in span and a 24 in chord driven by a mechanical shaker at the wing tip. Figure 13 shows dynamic AOAs at 86% span for shaker frequencies of 5 Hz and 12 Hz. The accuracy of the AOA measurements using the VMD system has been determined by comparing with a high accuracy rotational stage (1 arcsecond). The absolute errors in time-average AOA measurements by the VMD systems were found to vary from a few thousandths to a few hundredths of a degree over a 40^o range, depending on the position and orientation of the camera.

6. Conclusions

Photogrammetry is an essential ingredient of many image-based measurement techniques for wind tunnel testing. One problem in photogrammetry is the camera calibration, which determines the camera exterior and interior orientation parameters and lens distortion parameters. Photogrammetric applications in wind tunnels require a rapid single-station, single-image camera calibration method to maintain productivity. The optimization method developed in this paper enables camera calibration from a single image and does not suffer from a mathematical singularity problem. Combined with the DLT method to provide an appropriate initial guess, the method allows rapid automatic camera calibration. Laboratory experiments indicate that the optimization method compares favorably with proven optical techniques. The method has been successfully applied to temperature- and pressure-sensitive paints and model deformation measurements.

Acknowledgement: The authors would like to thank John C. Hoppe of NASA Langley and four reviewers for their helpful comments.

References

[1] McGlone, J.C., Analytic data-reduction schemes in non-topographic photogrammetry, Chapter 4, Non-Topographic Photogrammetry, 2nd Edition, (H.M. Karara, editor), American Society for Photogrammetry and Remote Sensing, Falls Church, Virginia, 1989, pp. 37-55.

[2] Wong, K.W., Basic mathematics of photogrammetry, Chapter 2, Manual of Photogrammetry, 4th Edition, (C.C. Slama, editor), American Society of Photogrammetry, Falls Church, Virginia, 1980, pp. 37-101.

[3] Wolf, P., Elements of photogrammetry, McGraw-Hill, New York, 1983, pp. 559-601.

[4] Donovan, J. F., Morris, M. J., Pal, A., Benne, M. E. and Crites, R. C., Data Analysis Techniques for Pressure- and Temperature-Sensitive Paint, AIAA Paper 93-0176, Jan. 1993.

[5] Bell, J. H. and McLachlan, B. G., Image registration for pressure-sensitive paint applications, *Experiments in Fluids*, 22, 1996, pp. 78-86.

[6] Le Sant, Y. and Merienne, M-C., An image resection method applied to mapping techniques, ICIASF '95 Record, International Congress on Instrumentation in Aerospace Simulation Facilities, Wright-Patterson Air Force Base, Dayton, Ohio, July 18-21, 1995, pp. 46.1-46.8.

[7] Burner, A. W., Radeztsky, R. H. and Liu, T., Videometric applications in wind tunnels, Videometrics V, Proceedings of The International Society for Optical Engineering (SPIE), Vol. 3174, San Diego, California, 1997, pp. 234-247.

[8] Liu, T., Radeztsky, R., Garg, S., and Cattafesta, L., A videogrammetric model deformation system and its integration with pressure paint, *AIAA Paper* 99-0568, Jan. 1999.

[9] Fraser, C.S., Photogrammetric camera component calibration --- A review of analytical techniques, Workshop on Calibration and Orientation of Cameras in Computer Vision (TU-1), XVII Congress, International Society of Photogrammetry & Remote Sensing, Washington, DC, 1992.

[10] Fryer, J. G., Camera calibration in non-topographic photogrammetry, Chapter 5, Non-Topographic Photogrammetry, 2th Edition, (H.M. Karara, editor), American Society for Photogrammetry and Remote Sensing, Falls Church, Virginia, 1989, pp. 59-69.

[11] Rüther, H., 1989, An overview of software in non-topographic photogrammetry, Chapter 10, Non-Topographic Photogrammetry, 2th Edition, (H.M. Karara, editor), American Society for Photogrammetry and Remote Sensing, Falls Church, Virginia, 1989, pp. 129-145.

[12] Tsai, R. Y., A versatile camera calibration technique for high-accuracy 3D machine vision metrology using off-the-shelf TV cameras and lenses, IEEE Journal of Robotics and Automation, Vol. RA-3, No. 4, August, 1987, pp. 323-344.

[13] Fraser, C.S., Optimization of networks in non-topographic photogrammetry, Chapter 8, Non-Topographic Photogrammetry, 2th Edition, (H.M. Karara, editor), American Society for Photogrammetry and Remote Sensing, Falls Church, Virginia, 1989, pp. 95-106.

[14] Abdel-Aziz, Y. I. and Karara, H. M., Direct linear transformation from comparator coordinates into object space coordinates in close-range photogrammetry, Proc. ASP/UI Symp. on Close-Range Photogrammetry, Univ. of Illinois at Urbana-Champaign, Urbana, Illinois, 1971, pp. 1-18.

[15] Cattafesta, L. W., III and Moore, J. G., Review and application of non-topographic photogrammetry to quantitative flow visualization, *AIAA Paper* 96-2180, June 1996.

[16] Pierre, D. A., Optimization theory with applications, Dover, New York, 1986, pp. 264-286.

[17] Burner, A.W., Snow, W.L., Shortis, M.R. and Goad, W.K., Laboratory calibration and characterization of video cameras, SPIE Vol. 1395 Close-Range Photogrammetry Meets Machine Vision, 1990, pp.664-671.

[18] Burner, A. W., Zoom lens calibration for wind tunnel measurements, Videometrics IV, Proceedings of The International Society for Optical Engineering (SPIE), Vol. 2598, Philadelphia, Pennsylvania, 1995, pp. 19-33.

[19] Dracos, T. and Gruen, A., Videogrammetric methods in velocimetry, *Applied Mechanics Reviews*, Vol. 51, No. 6, 387-413, 1998.

[20] Maas, H. G., Gruen, A., and Papantoniou, D., Particle tracking velocimetry in three-dimensional flows, *Experiments in Fluids*, 15, 133-146, 1993.

[21] MaLachlan, B. G. and Bell, J. H., Pressure-sensitive paint in aerodynamic testing, *Exp. Thermal and Fluid Science*, Vol. 10, pp. 470-485, 1995.

[22] Liu, T., Campbell, B., Burns, S. and Sullivan, J., Temperature- and pressure-sensitive paints in aerodynamics, *Applied Mechanics Reviews*, Vol. 50, No. 4, 227-246, 1997.

[23] Cattafesta, L. N., III, Iyer, V., Masad, J., King, R. A., and Dagenhart, J. R., Three dimensional boundary-layer transition on a swept wing at Mach 3.5, *AIAA J.* Vol. 31, No.3, pp. 2032-2037, 1995.

[24] Lin, R.-S, Masad, J., and Iyer, V., Computational study on the stability and transition of three-dimensional boundary layers on a swept wing at Mach 3.5, High Technology Report No. HTC-9606, June 1996.

[25] Cattafesta, L. N. III, Swept-wing suction experiments in the supersonic low-disturbance tunnel, High Technology Report No. HTC-9605, June 1996.

Appendix: Configuration Matrix and Observation Vector

The configuration matrix $\boldsymbol{A}$ and observation vector $\boldsymbol{l}$ in the linearized collinearity equations are

$$\boldsymbol{A} = \begin{pmatrix} (\partial f_1 / \partial \boldsymbol{\Phi}_{ex})_1 \\ (\partial f_2 / \partial \boldsymbol{\Phi}_{ex})_1 \\ \vdots \\ (\partial f_1 / \partial \boldsymbol{\Phi}_{ex})_M \\ (\partial f_2 / \partial \boldsymbol{\Phi}_{ex})_M \end{pmatrix} \text{ and } \boldsymbol{l} = -\begin{pmatrix} (f_1)_1 \\ (f_2)_1 \\ \vdots \\ (f_1)_M \\ (f_2)_M \end{pmatrix},$$

where the operator $\partial / \partial \boldsymbol{\Phi}_{ex}$ is defined as $(\partial/\partial\omega, \partial/\partial\phi, \partial/\partial\kappa, \partial/\partial X_c, \partial/\partial Y_c, \partial/\partial Z_c)$ and the subscript denotes the target. The components of the vectors $\partial f_1 / \partial \boldsymbol{\Phi}_{ex}$ and $\partial f_2 / \partial \boldsymbol{\Phi}_{ex}$ are

$$\frac{\partial f_1}{\partial \omega} = \frac{c}{W}\{ m_{12}(Z - Z_c) - m_{13}(Y - Y_c) - \frac{U}{W}[m_{32}(Z - Z_c) - m_{33}(Y - Y_c)]\},$$

$$\frac{\partial f_1}{\partial \phi} = \frac{c}{W}[-\cos\kappa\, W - \frac{U}{W}(\cos\kappa\, U - \sin\kappa\, V)] ,$$

$$\frac{\partial f_1}{\partial \kappa} = \frac{cV}{W} ,$$

$$\frac{\partial f_1}{\partial X_c} = \frac{c}{W}(-m_{11} + \frac{U}{W} m_{31}) ,$$

$$\frac{\partial f_1}{\partial Y_c} = \frac{c}{W}(-m_{12} + \frac{U}{W} m_{32}) ,$$

$$\frac{\partial f_1}{\partial Z_c} = \frac{c}{W}(-m_{13} + \frac{U}{W} m_{33}),$$

$$\frac{\partial f_2}{\partial \omega} = \frac{c}{W}\{ m_{22}(Z - Z_c) - m_{23}(Y - Y_c) - \frac{V}{W}[m_{32}(Z - Z_c) - m_{33}(Y - Y_c)]\},$$

$$\frac{\partial f_2}{\partial \phi} = \frac{c}{W}[\sin\kappa\, W - \frac{V}{W}(\cos\kappa\, U - \sin\kappa\, V)] ,$$

$$\frac{\partial f_2}{\partial \kappa} = -\frac{c\, U}{W} ,$$

$$\frac{\partial f_2}{\partial X_c} = \frac{c}{W}(-m_{21} + \frac{V}{W} m_{31}) ,$$

$$\frac{\partial f_2}{\partial Y_c} = \frac{c}{W}(-m_{22} + \frac{V}{W} m_{32}) ,$$

$$\frac{\partial f_2}{\partial Z_c} = \frac{c}{W}(-m_{23} + \frac{V}{W} m_{33}).$$

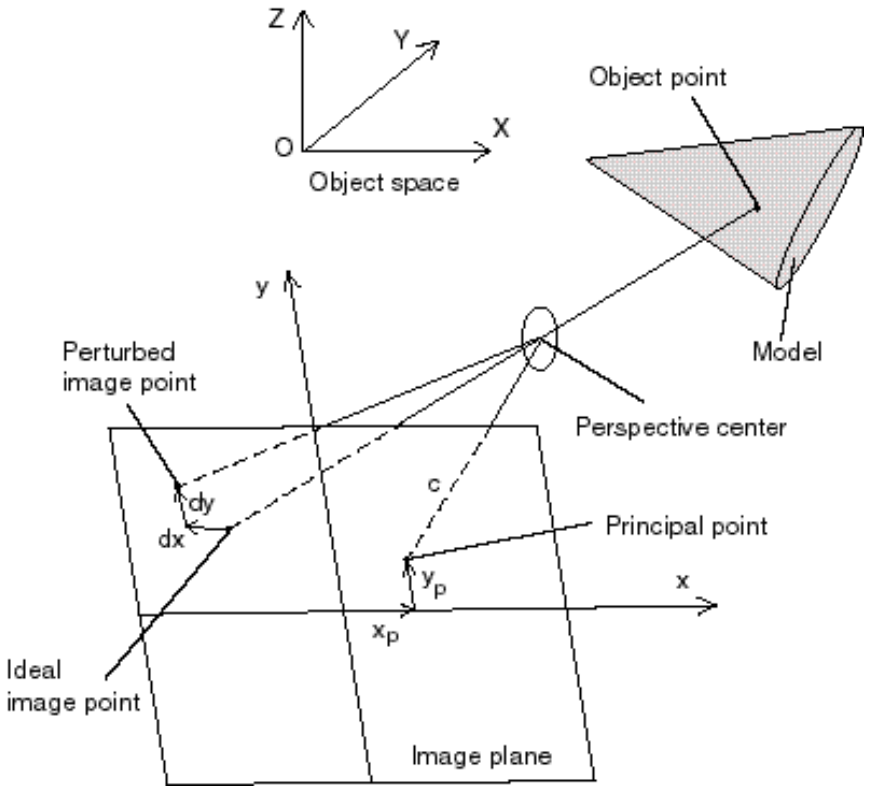

Figure 1. Camera imaging process and the interior orientation parameters.

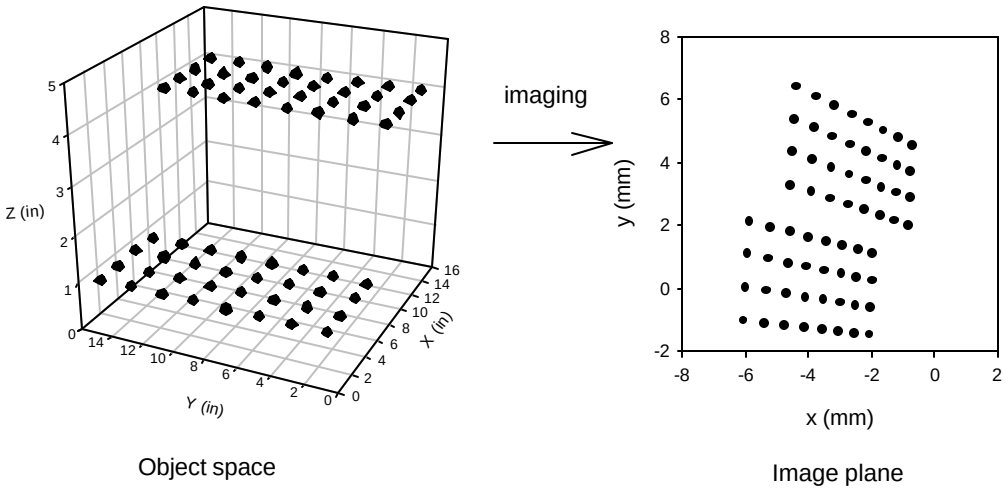

Figure 2. Target field on a step configuration and its image

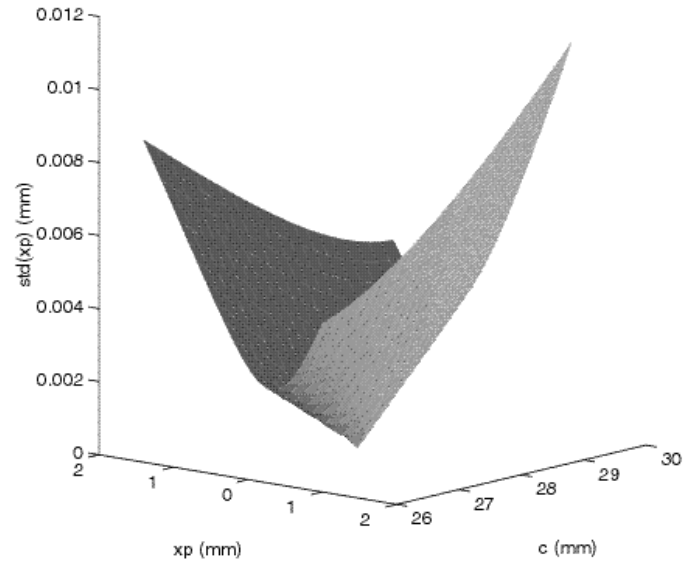

(a)

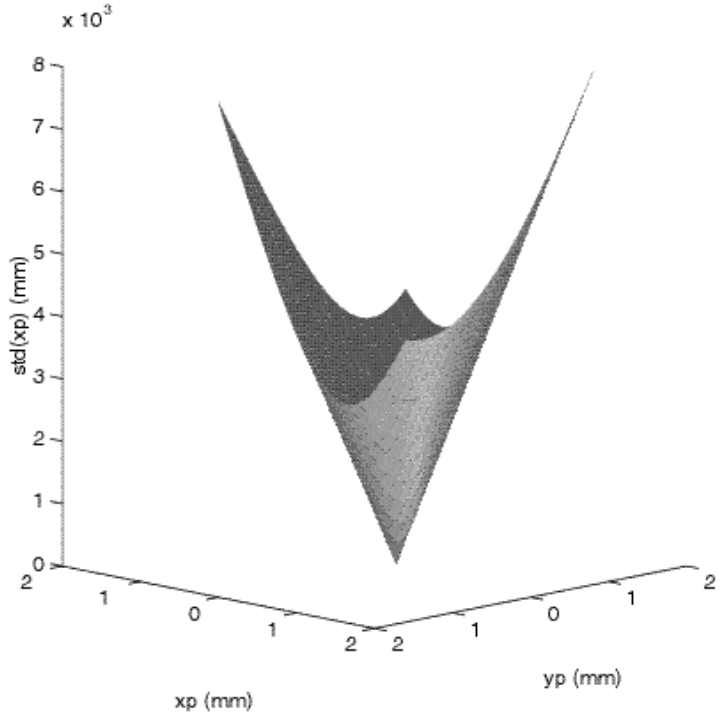

(b)

Figure 3. Topology of the objective function near the minimum point $(c, x_p, y_p) = (28, 0.2, 0.08)$ (mm).

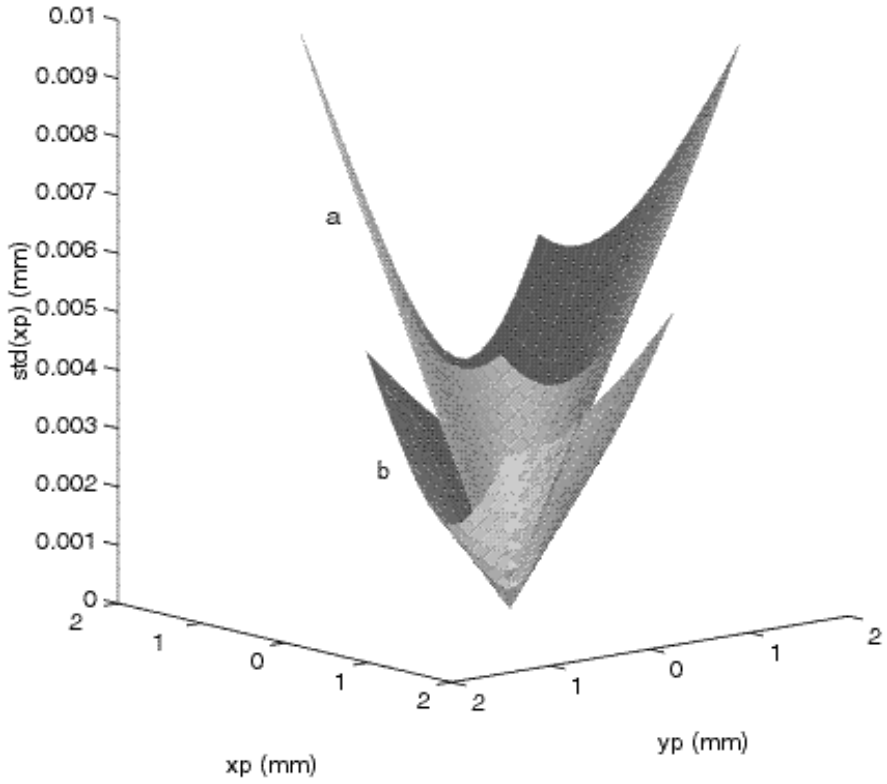

Figure 4. Effect of three-dimensionality (step height H) on topology of the objective function near the minimum point.
(a) H = 6 in, (b) H = 2 in.

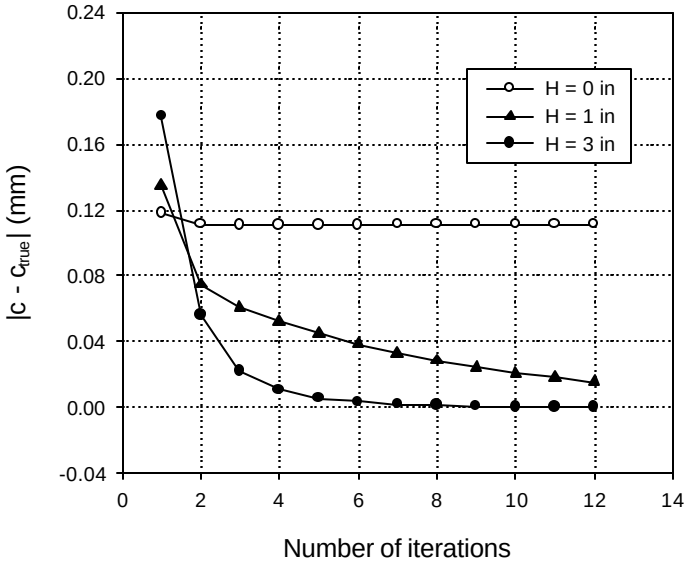

Figure 5. Effect of three-dimensionality (step height H) on convergence of the optimization solution.

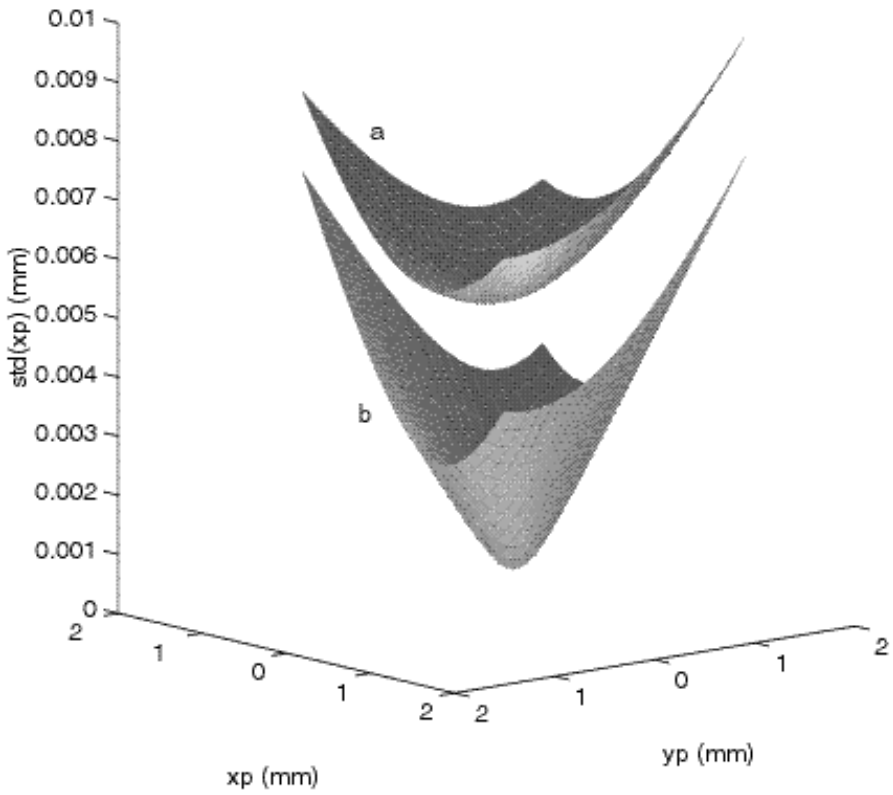

Figure 6. Effect of disturbance in image plane on topology of the objective function near the minimum point.
(a) disturbance level of 6 μm; (b) disturbance level of 1 μm.

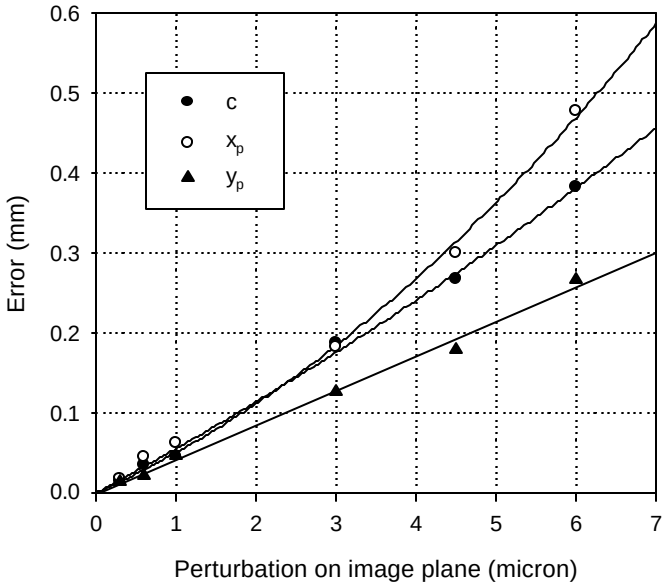

Figure 7. Errors in the interior orientation parameters as functions of disturbance level.

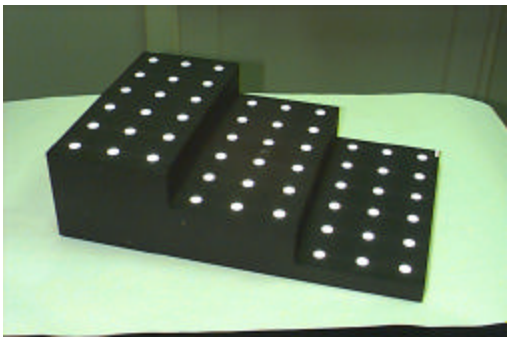

Figure 8. Step calibration target plate.

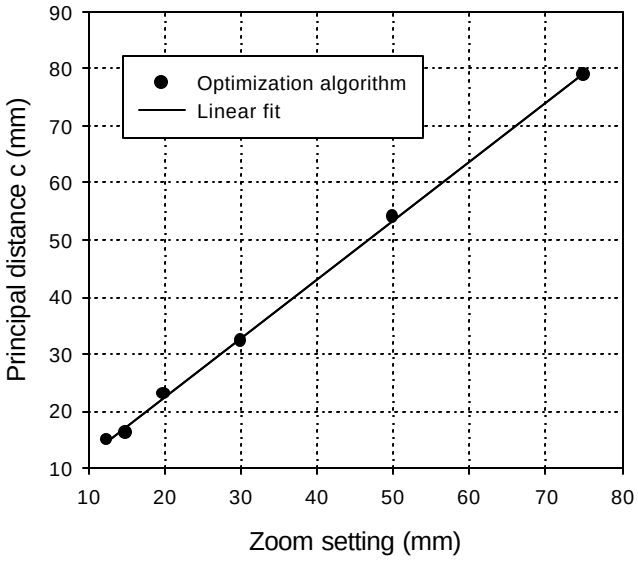

Figure 9. Principal distance vs. zoom setting for a Sony zoom lens

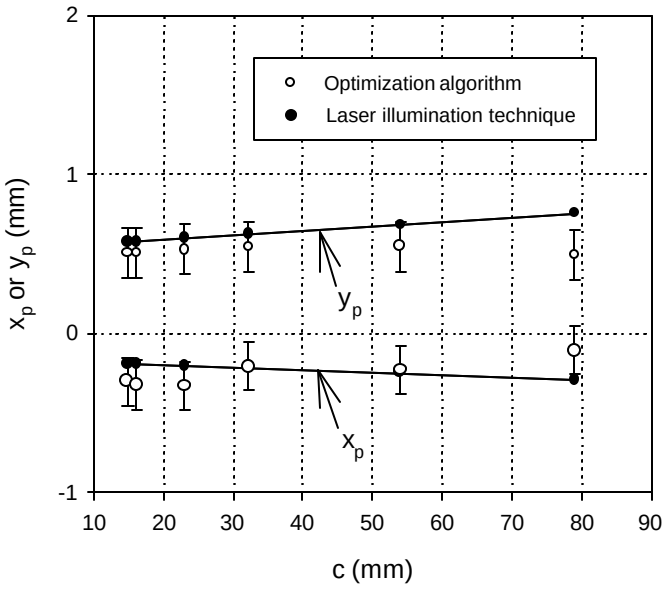

(a)

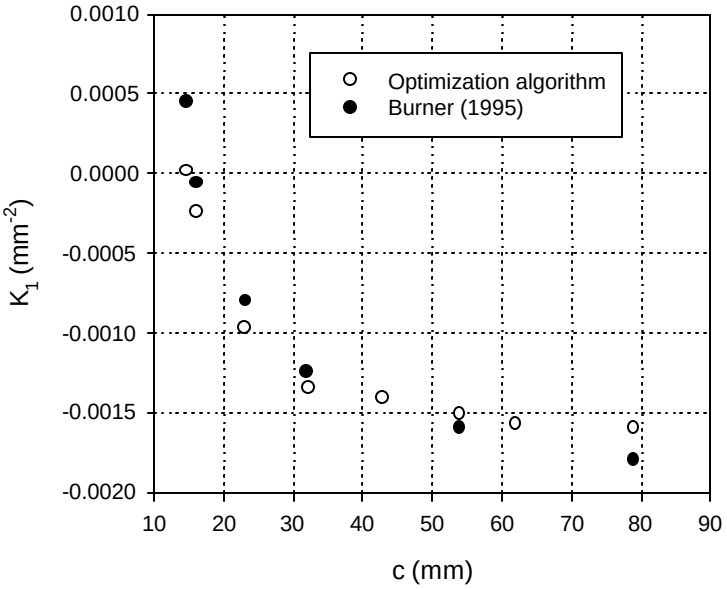

(b)

Figure 10. (a) Principal-point location and (b) radial distortion coefficient as a function of the principal distance for a Sony zoom lens connected to an Hitachi camera with an 8mm by 6mm CCD array.

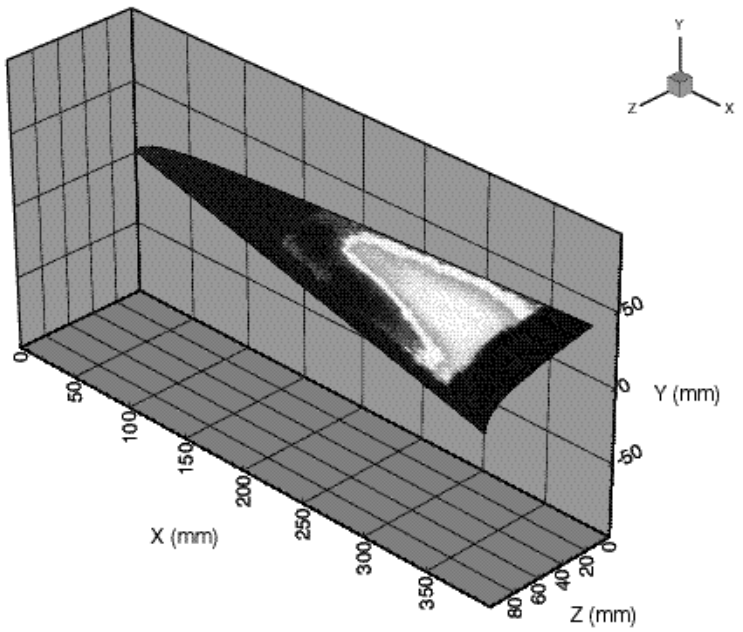

Figure 11. Result of photogrammetric mapping of transition image data to a half of the CFD grid of a swept-wing model at Mach 3.5.

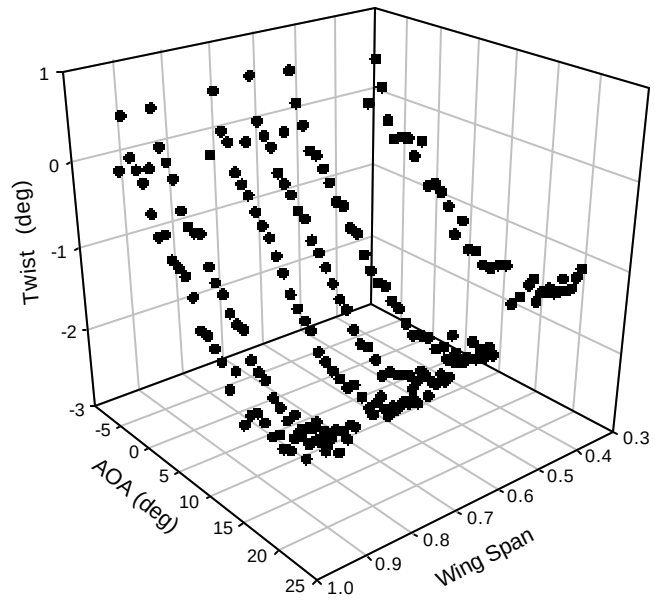

(a)

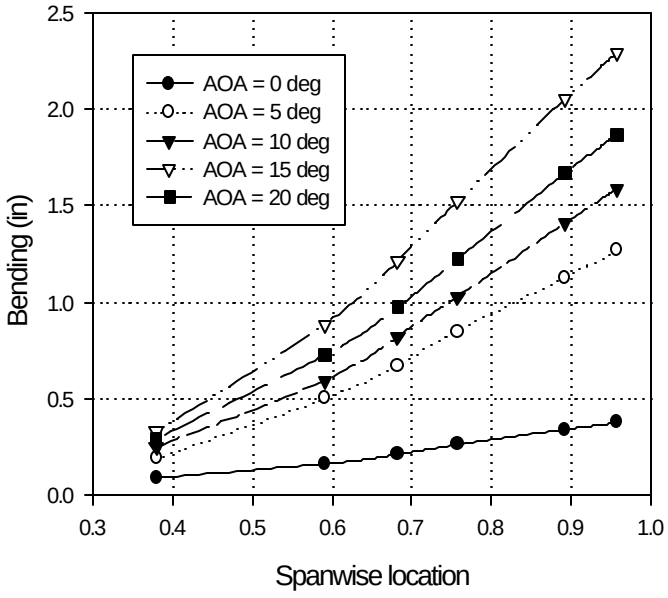

(b)

Figure 12. (a) Wing twist of a semi-span model as a function of AOA at different spanwise locations. (b) Wing bending at different spanwise AOAs.

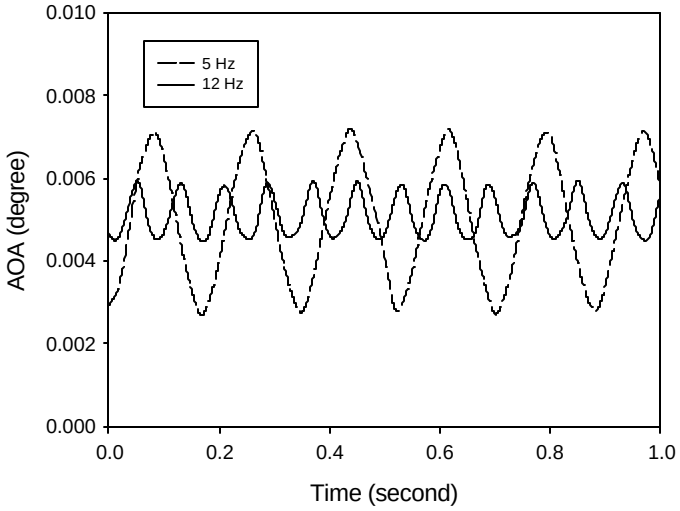

Figure 13. Dynamic AOAs of a rectangle wing measured by VMD at 86% span at 5 Hz and 12 Hz.